Selected Achievements and Discoveries Made in High-Enthalpy Flow Facilities

Hans G. Hornung

Graduate Aerospace Laboratories

California Institute of Technology

March 29, 2010

Contents

Report Documentation Page

1. REPORT DATE	2. REPORT TYPE	3. DATES COVERED
APR 2010	**N/A**	**-**

4. TITLE AND SUBTITLE	5a. CONTRACT NUMBER
Selected Achievements and Discoveries Made in High-Enthalpy Flow Facilities	5b. GRANT NUMBER
	5c. PROGRAM ELEMENT NUMBER

6. AUTHOR(S)	5d. PROJECT NUMBER
	5e. TASK NUMBER
	5f. WORK UNIT NUMBER

7. PERFORMING ORGANIZATION NAME(S) AND ADDRESS(ES)	8. PERFORMING ORGANIZATION REPORT NUMBER
Graduate Aerospace Laboratories California Institute of Technology	

9. SPONSORING/MONITORING AGENCY NAME(S) AND ADDRESS(ES)	10. SPONSOR/MONITOR'S ACRONYM(S)
	11. SPONSOR/MONITOR'S REPORT NUMBER(S)

12. DISTRIBUTION/AVAILABILITY STATEMENT
Approved for public release, distribution unlimited

13. SUPPLEMENTARY NOTES
See also ADA569031. Aerothermodynamic Design, Review on Ground Testing and CFD (Conception aerothermodynamique, revue sur les essais au sol et dynamique des fluides informatisee).

14. ABSTRACT

15. SUBJECT TERMS

16. SECURITY CLASSIFICATION OF:			17. LIMITATION OF ABSTRACT	18. NUMBER OF PAGES	19a. NAME OF RESPONSIBLE PERSON
a. REPORT **unclassified**	b. ABSTRACT **unclassified**	c. THIS PAGE **unclassified**	**SAR**	**26**	

1   Introduction

One path to scientific discovery is that a theoretical argument leads to a clear question that can be answered only by experiment. An experiment is a question asked of nature. If the question is asked in such a way that nature is able to answer it with a whole page, it is like the answer of a politician from which one is often left wondering what he said. The experiment therefore has to be formulated in such a way that nature is forced to say "yes" or "no". Of course, to be able to formulate the question in this manner, one has to know a good deal about the subject. So, in order to acquire such pre-knowledge, it is necessary to perform exploratory experiments (which nowadays can often conveniently be performed numerically) that serve to roam through the parameter space.

Another path is that, through physical exploratory experiments, phenomena are discovered that were previously not suspected, and that become explained theoretically only after their discovery. One variant of this path is that wrong ideas prevail over a considerable time, and only through persistent rubbing of the researcher's nose in the evidence can nature succeed in his final enlightenment.

In the following pages examples of both paths leading to new results will be presented. The word "new" in this context should be understood as "new at the time" because I will be presenting discoveries dating back to the 1970's. Since nearly all the major groups working in our field are represented at this lecture series, the contents will concentrate on the work of the groups with which I have been working.

Even from those the space and time limitations of this lecture make it necessary to omit a large number, including the work of Jean–Paul Davis on shock boundary layer interaction, the extensive work of Joe Olejniczak on the sensitive double cone flow, the detailed study of Ivett Leyva on shock detachment from a cone and the development of force measurement and two–body hypersonic flow by Stuart Laurence. Similarly, the important topic of development of instrumentation by Simon Sanderson and by Eric Cummings and the measurement of dissociation rates by Douglas Kewley are not discussed. The interested reader can find this work in publications under their names.

2   Shock Detachment

2.1   A Useful Gas Model

Vibrational excitation and chemical reactions in air can be quite complex, with many levels and many species and reactions, and much of the detail in the interaction of such processes with the gas–dynamical quantities can be captured satisfactorily by numerical computation. However, in this part of the lecture series we aim to explain the important phenomena with the simplest possible model that nevertheless captures the essential features. To this end, theoretical arguments are mostly based on the Lighthill–Freeman model of a dissociating symmetrical diatomic gas.

The equations of state and reaction rate model of this gas are stated here without derivation, as they are covered in detail in text books such as Vincenti and Kruger (1965).

The thermal and caloric equations of state are

$$p = (k/2m)\rho T(1 + \alpha) \tag{1}$$

$$h = (k/2m)[(4 + \alpha)T + \alpha\theta_d], \tag{2}$$

where p, ρ, h, and T are pressure, density, specific enthalpy and temperature, α is the mass fraction of dissociated gas, and k, m and θ_d are Boltzmann's constant, atom mass and characteristic temperature of dissociation. These two equations differ from the perfect gas form in the terms containing α in the thermal equation of state the α-term accounts for the increased particle number if the gas is partially dissociated. In the caloric equation of state the second term accounts for the enormous amount of energy that goes into dissociation. The Law of Mass action which defines the equilibrium composition is

$$\frac{\alpha^2}{1 - \alpha} = \frac{\rho_d}{\rho} e^{-\theta_d/T}, \tag{3}$$

where ρ_d is the equilibrium constant with the dimensions of density. The non–equilibrium behavior of the gas is modeled by the rate equation

$$\frac{d\alpha}{dt} = C\rho T^\eta \left[(1 - \alpha) e^{-\theta_d/T} - \alpha^2 \frac{\rho}{\rho_d} \right], \tag{4}$$

where C and η are constants defining the rate. The first term in the rate equation represents dissociation and the second recombination. Dissociation (proportional to ρ) and recombination (proportional to ρ^2) may be seen to be equal when the gas is in equilibrium, that is when equation (3) applies.

2.2   Normal and Oblique Shock

In order to calculate the behavior of flow through a normal shock with finite dissociation rate, equations (1), (2) and (4) describe the gas. For this purpose equation (4) is rewritten by observing that $u\,dt = dx$, u being gas velocity and x distance from the shock, in the form

$$u\frac{d\alpha}{dx} = C\rho T^\eta \left[(1 - \alpha) e^{-\theta_d/T} - \alpha^2 \frac{\rho}{\rho_d} \right]. \tag{5}$$

In addition the conservation equations for mass, momentum and energy need to be applied. These are:

$$\rho u = \rho_1 u_1 \tag{6}$$

$$p + \rho u^2 = p_1 + \rho_1 u_1^2 \tag{7}$$

$$h + u^2/2 = h_1 + u_1^2/2, \tag{8}$$

where the subscript 1 refers to conditions upstream of the shock. The result of integrating these equations with suitable values of the parameters is sketched in figure 1. The sketch suffices to get our main points across.

First, the gas properties jump across the shock giving the immediate post–shock conditions that correspond to frozen gas composition. This is followed by rapid dissociation with a rapid increase in α. This is accompanied by a rapid decrease of temperature because the dissociation is such a large energy sink, and an increase in density. Dissociation produces only a slight pressure rise. As α increases, the gas approaches closer
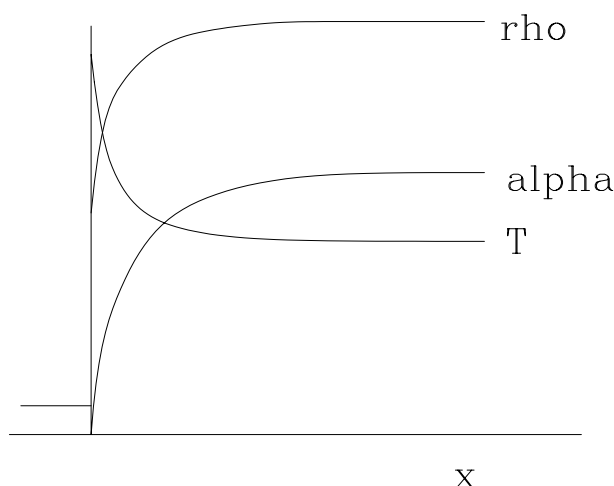

Figure 1: Sketch of the profile of properties over the distance from a normal shock in shock–fixed coordinates

to equilibrium and, accordingly, the rates of change of the gas–dynamical variables also decrease, all of them approaching the constant values corresponding to equilibrium. The distance behind the shock at which equilibrium is reached is called the relaxation length. An important feature is that the density ratio across a normal shock at equilibrium can reach typically twice the density ratio at the frozen shock. Thus, instead of a density ratio of 6 typical of a normal shock in a diatomic perfect gas, values up to 12 are typical at equilibrium.

The results for the normal shock may now be directly applied to the oblique shock, since the latter is obtained by superimposing a uniform flow on the normal shock. Thus, only the normal component of the velocity is affected. This may be illustrated as shown in figure 2.

By forming the magnitude of the velocity using $V = \sqrt{u^2 + v^2}$ we can now make a map of all possible end states of an oblique shock in the $V - \delta$ plane. Such a map is shown in figure 3
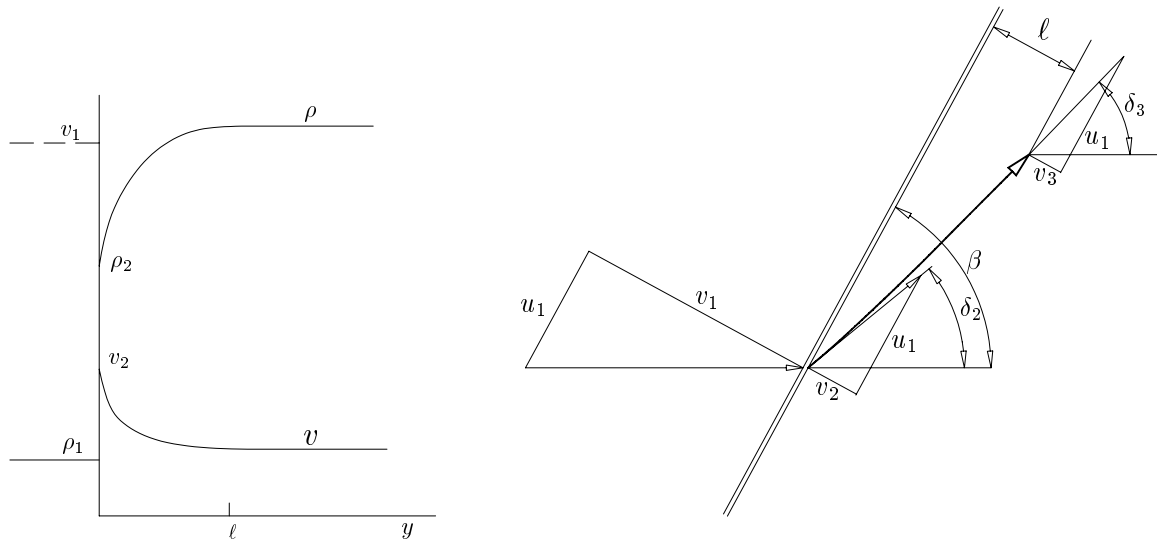
Figure 2: Left: Variation of density and normal velocity v over normal distance y from the shock, ℓ indicating relaxation length. Right: Superimposing a uniform flow u_1 parallel to the shock over a normal shock produces the oblique shock. Note that the decrease in v causes the deflection angle to change frome the frozen shock (subscript 2) to the equilibrium point (subscript 3).

The free–stream condition lies on the V–axis at the point $(1,0)$ (V is normalized by V_1) and the frozen and equilibrium normal–shock points also lie on the V–axis. M_2 and M_3 mark the maximum deflection points. The dashed line marks a shock with a particular shock angle, for which the frozen and equilibrium points are marked as 2 and 3.

2.3 Shock Detachment, Wedge

The $V - \delta$ map may now be used to discuss shock detachment. Recall that, if the shock angle is larger than the maximum deflection angle, the shock on a wedge will be detached from the tip of the wedge, forming a subsonic region behind a curved bow shock, with the sonic line emanating from the downstream wedge corner. The new situation of figure 4 now presents us with a paradoxical situation. The equilibrium maximum deflection angle is considerably larger than the frozen–flow maximum deflection angle. If the wedge angle lies between these two angles, is the shock detached or is it attached? According to the equilibrium locus, it is attached, and according to the frozen locus it is detached!

So now we have to ask ourselves how this contradiction can be reconciled. To this end consider the meaning of equilibrium, non–equilibrium and frozen flow. An observer who sees a flow as an equilibrium flow is one for whom the relaxation length ℓ is so small that he cannot resolve it. For an observer who sees a frozen flow the relaxation length is much larger than his window, so that he sees no composition change. The resolution of the paradox must therefore lie in a detachment distance that is too small for the equilibrium
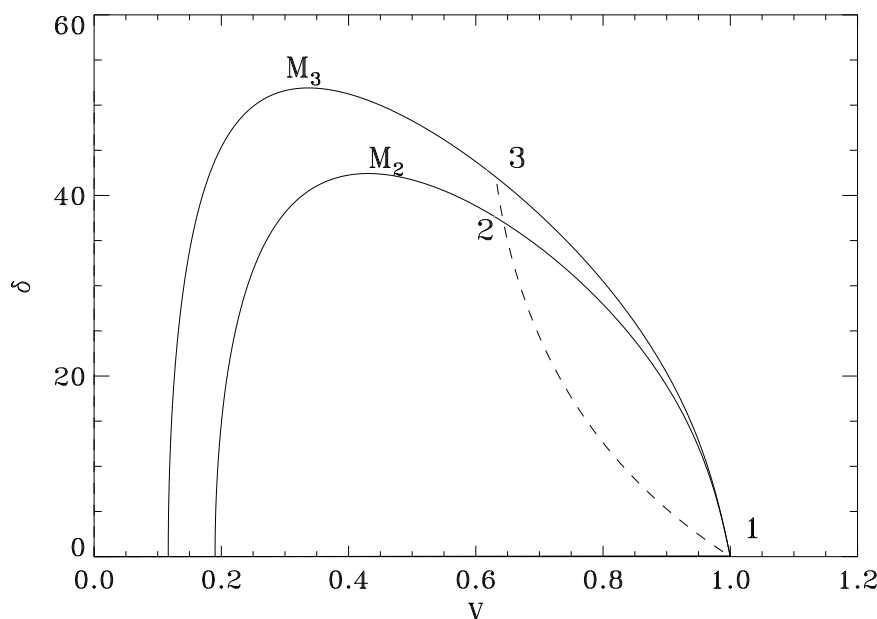
Figure 3: $V - \delta$ map of of frozen (2) and equilibrium (3) shock end states (full lines) and trajectory of a particular shock (dashed line). Quantitative integration of oblique shock for a particular set of parameters.

observer to resolve. This is illustrated in figure 4. On the left is shown a sketch of the flow over the wedge, and on the right a corresponding $V - \delta$ map, with the wedge angle between the two maximum deflection points. Region A on the left maps into the free–stream point A' on the right. The stagnation streamline maps into a line that passes through the two normal–shock points to the origin, then jumps along the δ–axis to δ_w and from there to C'. The far–field streamline BC maps into the oblique shock solution B'C', and a streamline entering close to the stagnation streamline at the point D maps into the curved line D'C'. Thus, if now were to represent the shock for an equilibrium observer by a thick region larger in width than ℓ, the shock would appear to be attached, while those who can resolve ℓ see a small detached region embedded in the relaxation region.

It is necessary to discuss the behavior of the sonic line. The map of the sonic line is shown in figure 4 on the right as a dashed line. Since the shock stand-off distance Δ scales as the size of the subsonic region, this too must be of similar extent as ℓ as the equilibrium observer who sees the shock as attached must not be able to resolve it. This suggests a location of the sonic line as shown on the left. It implies that a subsonic region can terminate on the straight wedge face, a situation that is not possible in a perfect gas flow. In fact it is possible to show that a straight shock with relaxation exhibits a range of shock angles within which there exists a thin subsonic region close to the shock.

Figure 5 shows the predicted behavior of the stand-off distance according to our theoretical argument, with Δ remaining small while the wedge angle lies between the two maximum deflection points and jumping to the equilibrium behavior when the wedge angle exceeds the equilibrium maximum deflection point. This may be seen to be mirrored
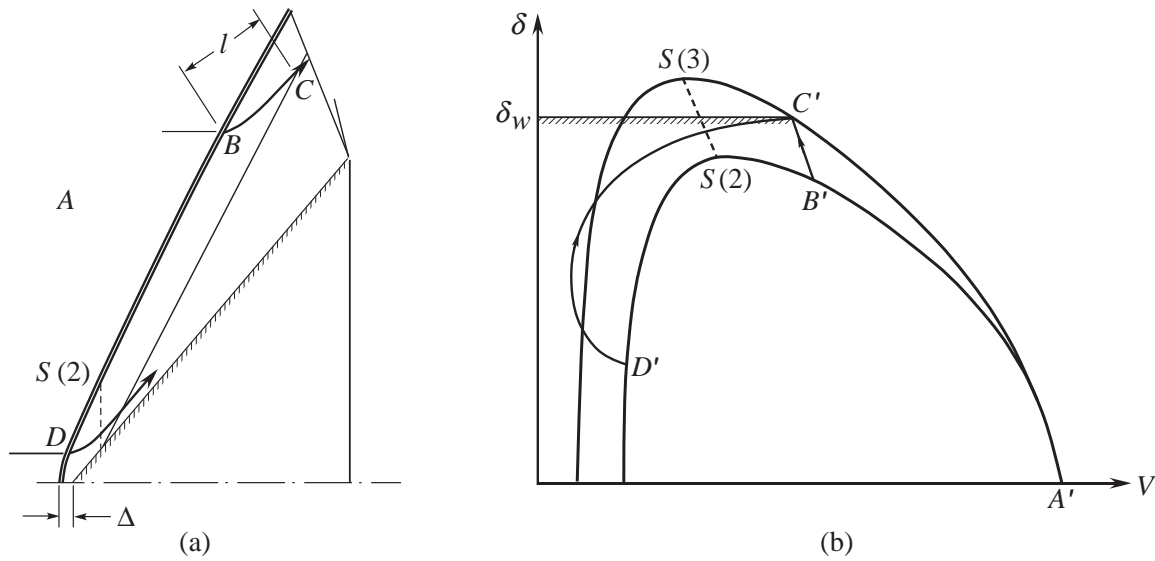
Figure 4: Left: Sketch of physical flow over a wedge in the case when the wedge angle lies between the frozen and equilibrium detachment angle. The thin line that is almost parallel to the shock represents the end of the relaxation region of flow length l. The dashed line is the sonic line. Right: $V - \delta$ map of the flow on the left showing the mapping of marked points, streamlines and sonic line from the physical plane to the $V - \delta$ plane.
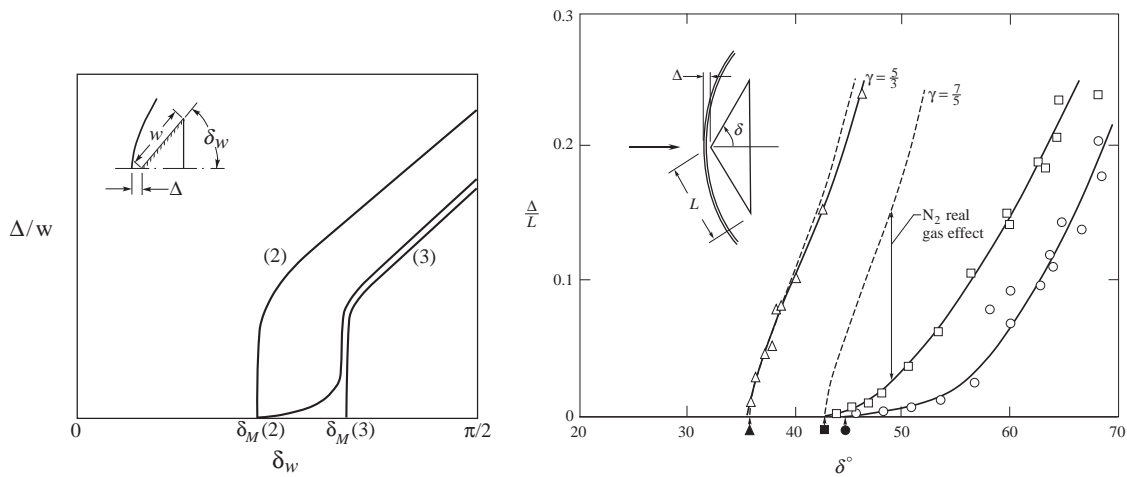

Figure 5: Left: Behavior of the stand-off distance according to the theoretical argument with what the frozen observer (2), the equilibrium observer (3) and an observer who resolves both will see. Right: Measured behavior, triangles, argon perfect gas; squares, nitrogen dissociating; circles, carbon dioxide dissociating. Full lines, faired curves through experimental points. Dashed line, frozen behavior. Filled symbols with arrows, frozen detachment points. After Hornung and Smith (1979).

in the experimental results on the right of the figure, showing that the stand-off distance increases very gradually for relaxing flow, while it takes off quite suddenly in the perfect gas case. Also the larger energy sink of dissociating carbon dioxide compared with that

of nitrogen is clearly in evidence. These experiments were performed in the free–piston shock tunnel T3 at the Australian National University.

The effect of relaxation on shock detachment from a cone was shown to be equally predictable and equally dramatic as in the case of the wedge by Hornung and Houwing (1980) and by Leyva (1999).

3   Blunt Body Flows

3.1   Curved Shock

In flow without relaxation (such as perfect–gas or frozen or equilibrium flow) the conditions downstream of a plane shock are spatially uniform. We have seen in the previous sections that relaxation introduces spatial gradients in the flow properties immediately downstream of the shock. Spatial gradients also occur in flows without relaxation if the shock is curved. There are thus two agencies that introduce gradients downstream of a shock: relaxation and shock curvature.

Consider a curvilinear coordinate system with origin at a point where a streamline of our interest crosses the shock and with the x-axis along the shock as shown in figure 6. Hornung (2010) obtained the gradients of flow properties immediately downstream of the
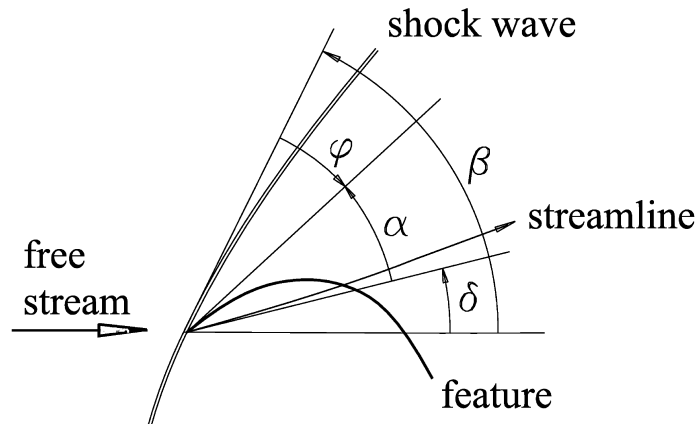

Figure 6: Sketch of flow plane, also defining angles that will be used later. The double line is the shock, the heavy line is some feature, *e. g.*, a density contour. The angles ϕ and α measure the direction of the feature at the shock wave relative to the shock and relative to the streamline, respectively. δ is the deflection angle of the streamline at the shock.

curved shock by differentiating the shock jump conditions with respect to x and solving for the y–derivatives from the equations of motion. While this work obtained shock jump relations for the gradients of many variables in the general case of a three–dimensionally curved shock, we restrict the discussion to two–dimensional flow one variable. The y–components of the gradients of flow quantities may be expressed in the form

$$
\begin{aligned}
p_y &= A_{(p)}(M,\gamma,\beta)\, r + C_{(p)}(M,\gamma,\beta)\, k & (9) \\
u_y &= C_{(u)}(M,\gamma,\beta)\, k & (10) \\
v_y &= A_{(v)}(M,\gamma,\beta)\, r + C_{(v)}(M,\gamma,\beta)\, k & (11) \\
\rho_y &= A_{(\rho)}(M,\gamma,\beta)\, r + C_{(\rho)}(M,\gamma,\beta)\, k, & (12)
\end{aligned}
$$

where the A's and C's are explicitly known functions of the free–stream Mach number M and specific heat ratio γ, and the shock angle β. As expected, each y–derivative has contributions arising from the chemical reaction rate r and the shock curvature k. All the

x–derivatives have contributions only from k. It should be pointed out that, although the relaxation rate may involve many modes of vibration and reactions between many species, the flow variables are influenced by relaxation only through the rate of energy absorption and may therefore be lumped into the single parameter r. Of course, the dependence of r on temperature and density can only be obtained from the details of the relaxation process. The gradient of density is particularly sensitive to reaction rate. This is shown for a particular set of parameters in figure 7. In a qualitative way this behavior can be
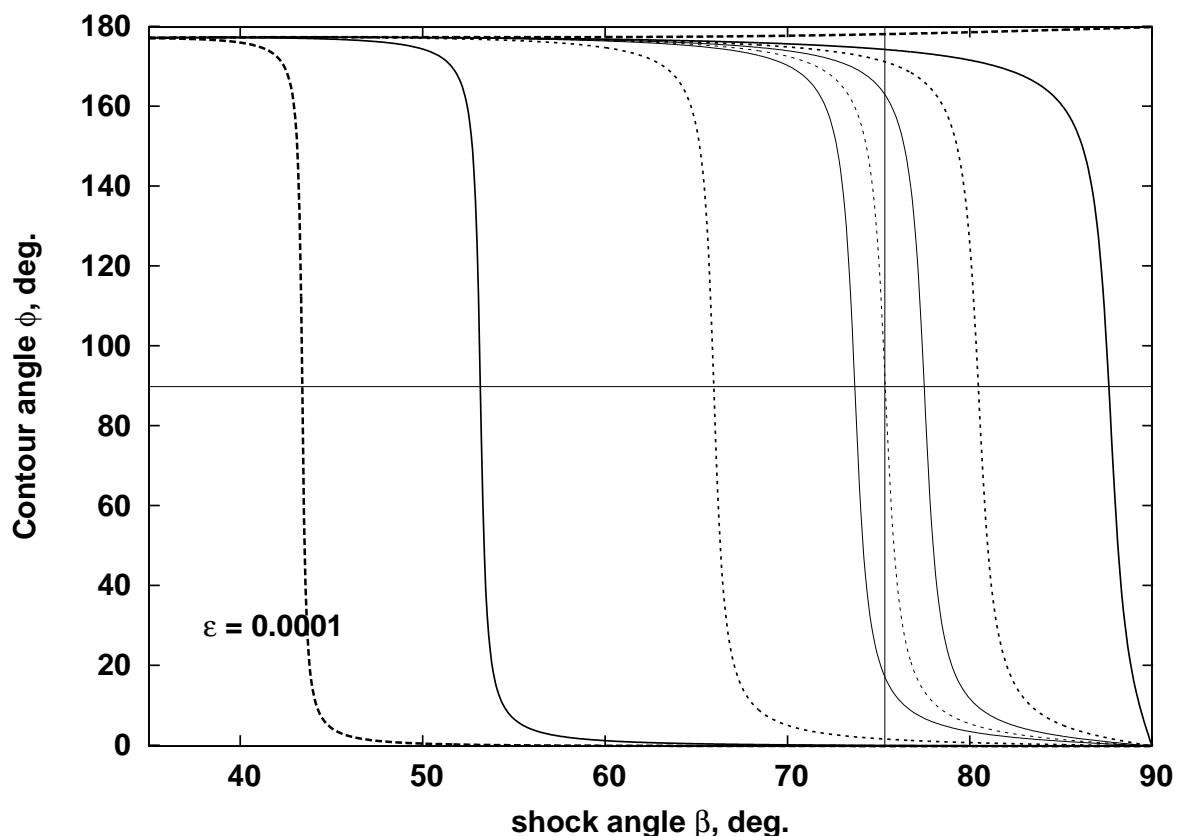

Figure 7: The curves show the behavior of $\phi(\beta)$, the angle between the shock and the density contour, for different values of dimensionless reaction rate ε: 10^{-4}, 10^{-3}, 10^{-2}, 10^{-1}, 10, -10^{-1}, -10^{-2}, -10^{-3}, -10^{-4}, in heavy broken, full, broken, light full, light broken, light full, broken, full, heavy broken lines, respectively, so that the leftmost heavy broken curve corresponds to a high dissociation rate, the light broken curve corresponds to frozen flow ($r = 0$), and the curves to the right of the light broken curve correspond to exothermic reaction ($r < 0$).

seen in the interferograms shown in figure 8.   A striking feature about the behavior of the angle between the density contour and th e shock is that, at small shock angles, which occur far downstream on the bow shock of a blunt body, ϕ is approximately 180°, then, at a particular value of e̲ta it switches relatively suddenly to 0 at large shock angles, which occur near the stagnation streamline of a blunt body. Also, the shock angle at the switching angle is very sensitive to the reaction rate. The switching point manifests itself in a half saddle point in the density field.
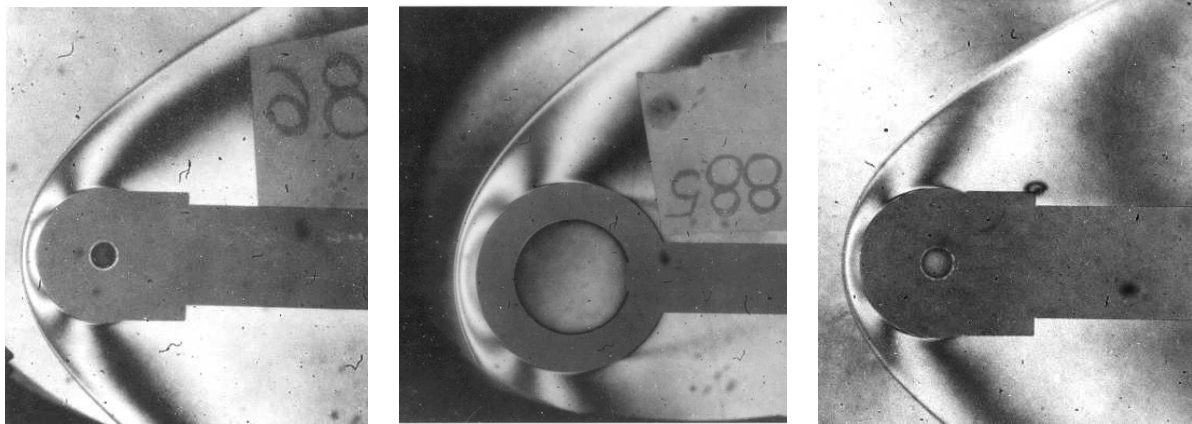
Figure 8: Infinite–fringe interferograms of flows over a circular cylinder in the presence of dissociation from experiments performed in the T3 shock tunnel by Hornung (1972). LEFT: Nitrogen flow over a 25.4 mm diameter cylinder at a speed of 5.59 km/s, density 0.005 kg/m^3. The value of β at the half saddle is approximately 49°, corresponding to $\varepsilon \simeq 1.5 \times 10^{-4}$ MIDDLE: Same free–stream conditions, but with a cylinder diameter of 50 mm, corresponding to a doubling of r. This is nicely reflected in the change of the value of the value of β at the half saddle from 49° to 45°. RIGHT: Carbon–dioxide flow over the same cylinder as in the left picture. $V_\infty = 3.6$ km/s, $\rho_\infty = 0.0016$ kg/m^3. In this case r is so large that the half saddle is moved to such small shock angles that it does not appear within window.
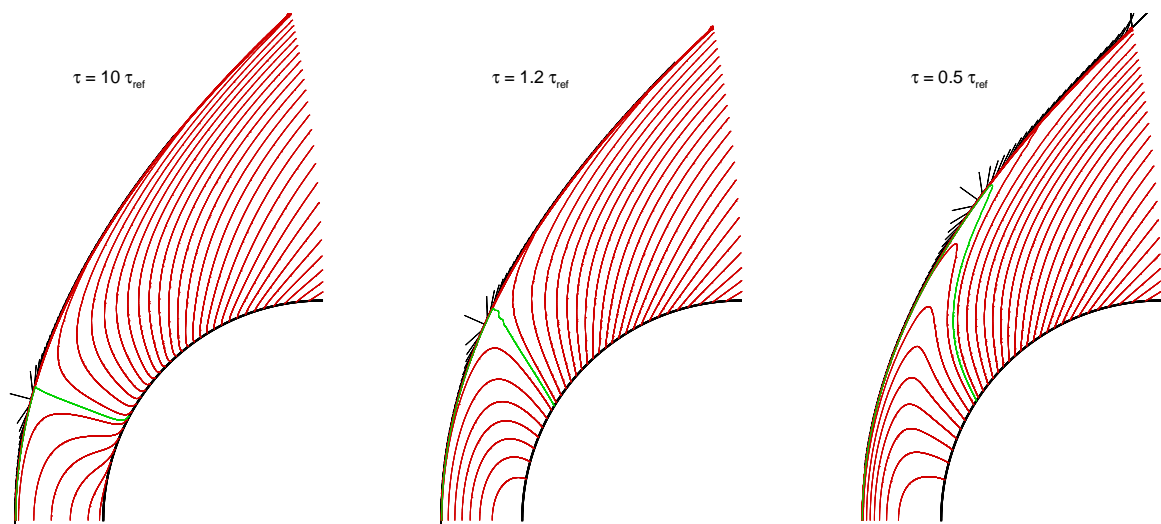

Figure 9: Computed lines of constant density in flow over a circular cylinder with vibrational relaxation. Three cases with different relaxation times τ are shown. The directions of the contour lines as obtained from the theory are shown as short lines on the upstream side of the shock. Note that, though the location of the half saddle of the computation is close to but not exactly at the computed location. From Candler (2010).
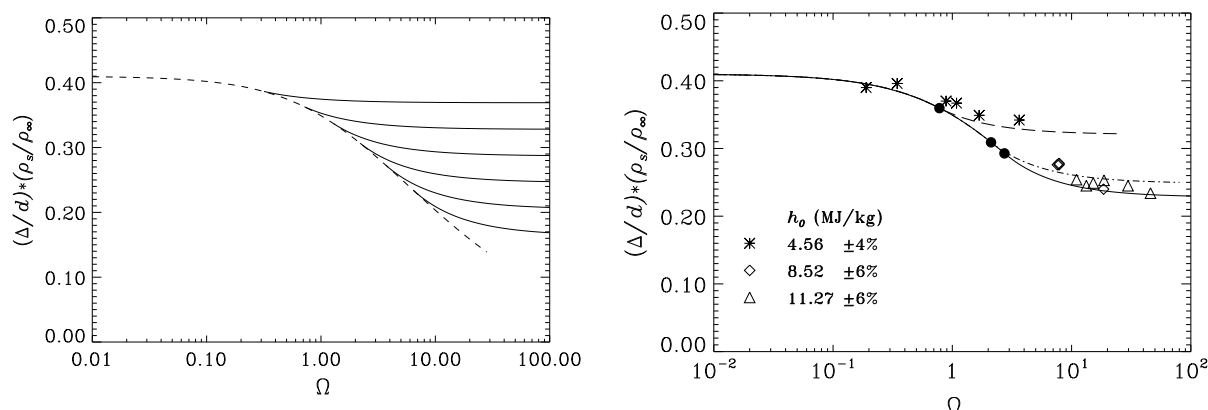
Figure 10: LEFT: Theoretical behavior of shock stand–off distance on a sphere with dimensionless reaction rate parameter Ω with density ratio ρ_e/ρ_s as a parameter. RIGHT: Comparison of the theory with experimental carbon dioxide flows in T5 at three reservoir specific enthalpies h_0. Changing h_0 causes a change in ρ_e/ρ_s. From Wen and Hornung (1995).

The sensitivity of the half saddle location to relaxation rate was also demonstrated in a computational study by Candler (2010) in which he compared the theoretical value of ϕ with the computed density field in flow with vibrational relaxation. It was necessary to fit a curve to the computed shock in order to obtain a smooth value of the shock curvature. Some of his results are shown in figure 9. They show very nicely the shift of the half saddle to smaller β as τ is reduced and illustrate how sensitive this location is to relaxation rate.

3.2   Shock Stand-Off Distance

One of the consequences of the increase of density brought about by dissociation after a normal shock is that the distance from the bow shock wave to the stagnation point on a blunt body is drastically reduced. Experiments in the T3 shock tunnel and computations (Hornung (1972)) showed that the stand–off distance in nitrogen flows can be reduced by as much as a factor of two by this effect. It was through these results that the sensitivity of the density field to non–equilibrium effects was discovered, including the movement of the half saddle poing discussed in the previous section.

However, at that time Hornung (1972) incorrectly stated that the dimensionless shock stand–off distance depended only on a single dimensionless reaction rate parameter It should have been obvious that a second parameter measuring dimensionless equilibrium density ratio across the shock would play a role. The situation was rectified by Wen and Hornung (1995), who showed that the dimensionless stand–off distance could be expressed in terms of the dimensionless reaction rate and the ratio ρ_e/ρ_s where ρ_e is the density at equilibrium after a normal shock and ρ_s is the density immediately after the shock before any relaxation occurs. This ratio is also a measure of the dimensionless energy absorption by relaxation. They also obtained extensive experimental results performed in the T5 shock tunnel at Caltech. An example of their results is shown in figure 10.
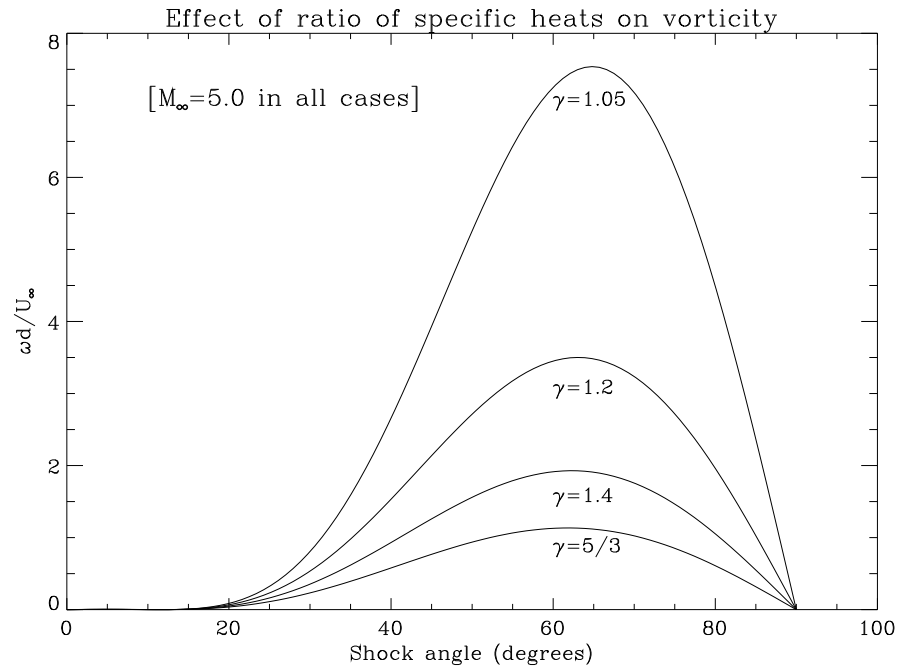
Figure 11: Dimensionless vorticity generated by the bow shock on a sphere in perfect–gas flow at $M = 5$. The effect of γ on the density ratio is the cause of the rapid increase of vorticity as γ approaches 1. From Hornung and Lemieux (2001).
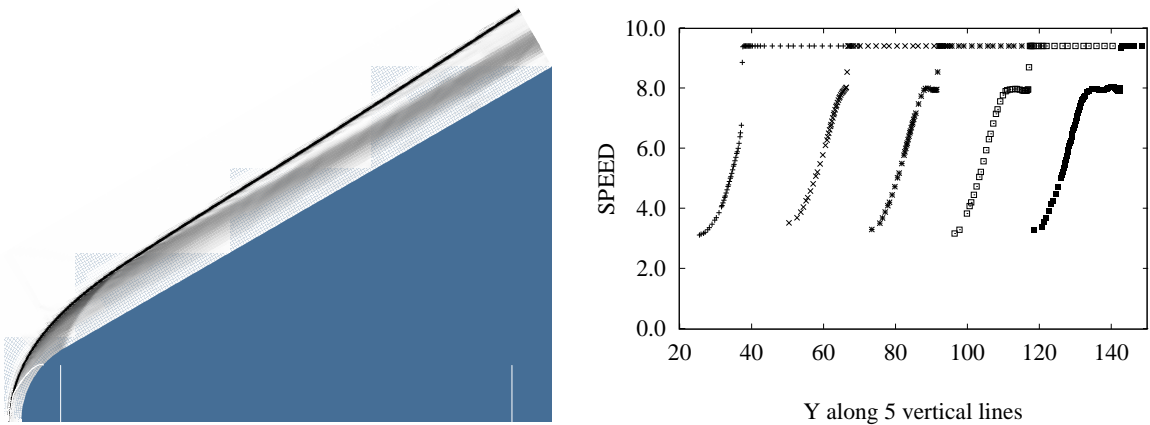

Figure 12: Left: Euler computation of flow over a cylindrically blunted wedge ($M = 9$, $\gamma = 1.095$). Right: Speed distribution along 5 equally spaced vertical lines, showing a layer with large vorticity.

3.3   Shear Layer Instability

A curved shock, generated, for example, as the bow shock of a blunt–nosed body in a steady, uniform free stream, generates vorticity

$$\omega = U_\infty \kappa \cos \beta \left(1 - \frac{\rho_\infty}{\rho} \right)^2 \frac{\rho}{\underline{\quad}}$$

by the baroclinic mechanism within the shock wave. Here, U_∞, ρ_∞ are free–stream speed and density, and β, κ are the shock angle and curvature at the point of interest. In the case of a perfect gas flow at $M = 5$ over a sphere, for which the shock may be approximated by a hyperboloid, the vorticity may be obtained as a function of β and γ as shown in figure 11. As an example of this, figure 12 shows a pseudo-schlieren image of an
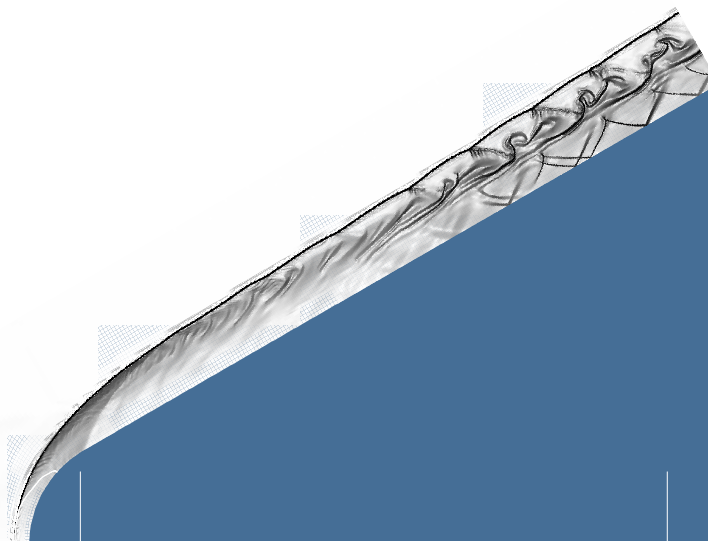

Figure 13: Example of growth of disturbance introduced in the free stream, in the case when the normal–shock density ratio is approximately 20 and the disturbance wavelength is one nose radius. Note the shock waves pushed by the shear layer structures and the distortion of the shock.

Euler computation of flow over a cylinder–wedge and corresponding speed distributions across the shock layer. In this plane flow, the shear layer generated by the shock lies at an approximately constant distance from the body, while in a similar axisymmetric flow the vortex stretching would cause the vorticity maximum to lie at the body surface and increase in value, see Hornung and Lemieux (2001).

Shear layers eventually become unstable. How far they travel before becoming unstable depends in part on the magnitude of the vorticity in the layer. In order to check out the conditions under which the shear layer becomes unstable within a few nose radii from the nose of a blunt body, we did the following exploratory experiment by computation. In the free stream of the flow shown in figure 12 introduce a disturbance in the form of a small oscillating velocity component normal to the symmetry plane, whose amplitude varies smoothly from zero on the axis to a maximum near where the shock angle is about 60° and decreasing smoothly to zero in the far field. By performing many such computations we discovered the following results:

Instabilities develop in the shear layer within the computational window only if the normal–shock density ratio is larger than 14. The most unstable wavelength lies in the region of one nose radius, although this maximum is quite broad. The shear layer structures convect supersonically relative to the flow near the surface, so that they push shock waves that reflect from the surface, the reflections re–interacting with the shear layer.

The shear layer structures can be sufficiently strong to distort the main shock. The last two mechanisms provide a non–linear growth for the structures. An example of the flow that results is shown in figure 13.
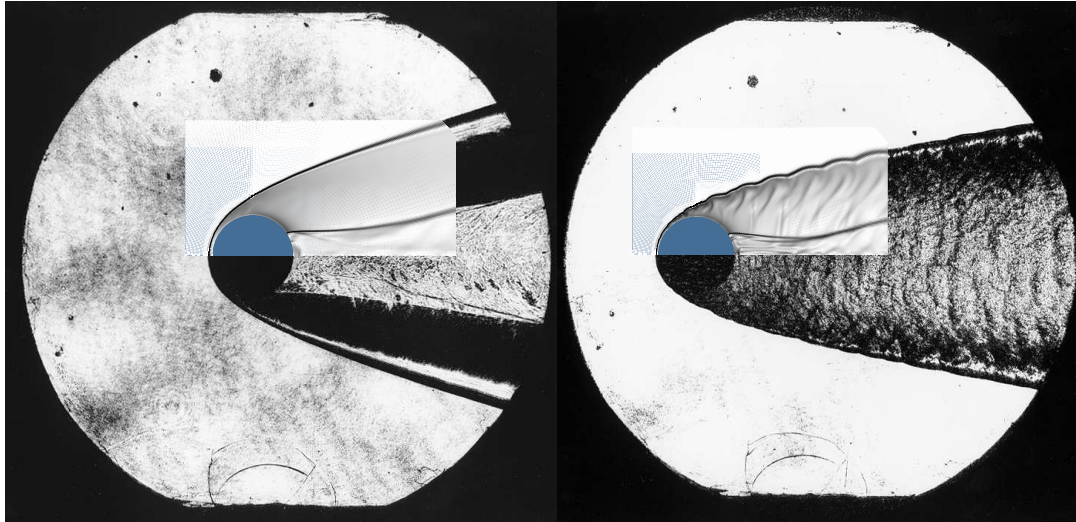

Figure 14: Results of the physical "yes/no" experiment. Left: Propane, $U_\infty = 1.26$ km/s, normal–shock density ratio 12. Note that, because the shadography system was set up with extreme sensitivity, the region of highest density gradient appears black in this image. Right: Propane, $U_\infty = 2.7$ km/s, normal–shock density ratio 20. In both images computational results are superimposed. The conditions for the computations are chosen to give the same normal–shock density ratios. Of course, the shadowgraphs are line–of–sight integrating, while the computational inset show density gradients in a slice. From Hornung and Lemieux (2001).

Armed with these results it was time for us to do the physical "yes/no" experiment. Unfortunately it is not possible to generate a flow in the reflected shock tunnel in which relaxation effects cause an increase of the normal–shock density ratio to 14 or more. (Note that this limitation does not apply to expansion tubes). However, Joe Shepherd and his student Mike Kaneshige had modified the T5 shock tunnel to convert it into a gun with which a 25 mm diameter nylon sphere could be propelled into a small test section at the far end of the dump tank in order to study projectile generated oblique detonation waves in hydrogen–air mixtures. By filling this test section with propane or carbon dioxide and shooting the nylon sphere through it with a speed of 2.7 km/s, it was easily possible to obtain density ratios of up to 20.

Figure 14 shows two shadowgraphs taken in this facility with the nylon sphere fired into propane at 1.26 (left) and 2.7 km/s (right) corresponding to normal shock density ratios of 12 and 20 respectively. The shock wave and flow features are smooth in the left image and obviously very significantly disturbed in the one on the right. The wake shock can be seen quite clearly in the left image and it is hidden somewhat by the turbulent nature of the flow in the one on the right. The large disturbance in the flow on the right is sufficient to distort the shock wave. Superimposed on these shadowgraphs are pseudo–schlieren images of computed flow field at appropriate conditions. These show the wake

shocks rather more clearly because they are radial slices through the flow rather than line–of–sight integrating images which the shadowgraphs are.

3.4   Shock–shock interaction

In order to examine the effect of relaxation on Edney's Type IV shock–on–shock interaction, which Edney had speculated would increase the heat flux amplification to as much as a factor of 60 from the factor around 15 that he measured in a diatomic perfect gas, Sanderson (1995) (see also Sanderson et al. (2004)) studied this phenomenon in T5 with dissociating nitrogen flow over a circular cylinder. The impinging shock was very elegantly generated by a waverider. Without going into detail, these experiments showed the amplification to be much more benign. An example of Sanderson's extensive collection of very beautiful holographic interferograms is shown in figure 15.
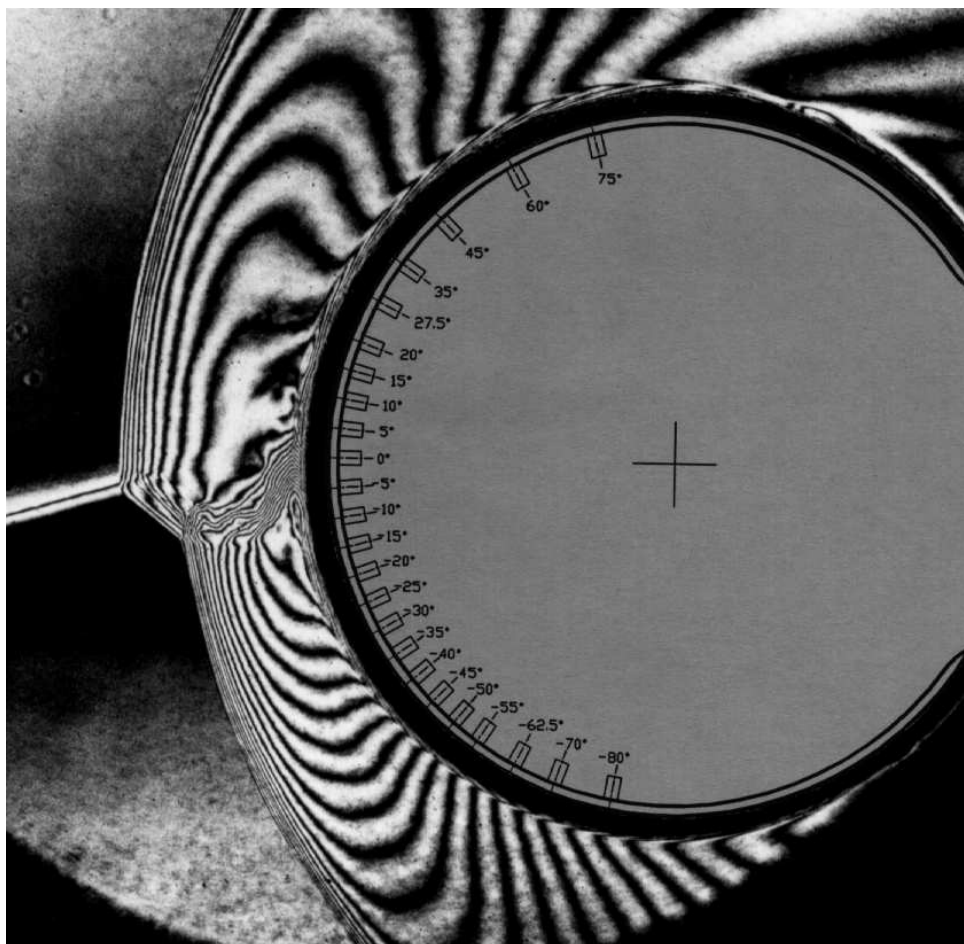

Figure 15: Holographic infinite fringe interferogram of Edney Type IV interaction in dissociating nitrogen flow. Note the exquisite detail visible even in the region where the jet impinges on the body. Also note that, as in the middle image of figure 8, the separation at the back of the cylinder is clearly evident. From Sanderson (1995). I doubt whether a more beautiful image of dissociating hypersonic flow exists.

4   Boundary Layer Transition

4.1   Introduction

Heat loads and forces on hypervelocity vehicles depend critically on the location of transition from laminar to turbulent flow. Though significant progress has been and is being made toward the understanding of transition, it is still the most severe uncertainty in the aerodynamic design of such vehicles.

Two important features of hypervelocity flow set it apart from other flow regimes with respect to the transition problem. First, the dominant instability mode at sufficiently high Mach number is the second or Mack mode (see Mack (1969)), in which acoustic disturbances become trapped in the boundary layer, grow in amplitude and eventually cause the boundary layer to become turbulent. This is in contrast to the situation in low speed flows, where the viscous instability is usually responsible for the path to transition. Second, the relaxation processes associated with vibrational excitation and dissociation (which occur in hypervelocity flows because of aerodynamic heating) provide mechanisms for damping acoustic waves, and may therefore be expected to affect the second mode. The effects of vibrational excitation and dissociation are quite subtle however, since they also affect the mean structure and therefore the stability properties of the boundary layer.

A large part of the experimental work on the problem of stability and transition at high Mach number has been done in cold hypersonic facilities. Reshotko (1976) presented a very good review of this body of work. Together with the linear stability analysis by Mack (1969), cold hypersonics experiments provide a substantial basis for understanding the path to transition hypersonic flow. They are, however, not able to capture the phenomena that occur in high–enthalpy flows because of the vibrational excitation and dissociation that characterize them.

Some of the specific problems of high–enthalpy boundary layer stability have been addressed computationally by a number of authors. They include the work of Malik and Anderson (1991), who considered equilibrium vibration and dissociation, and Stuckert and Reed (1994) who assumed vibrational equilibrium but finite-rate chemistry. Both found that the new effects caused the boundary layer to be destabilized. However, more recent work by Johnson et al. (1998) found that non-equilibrium chemistry had a strong damping effect, in agreement with recent experimental evidence. The apparent contradiction between the results of these investigations is not too surprising in view of the complicated manner in which the rate processes can influence the stability problem, and the many parameters involved in it.

In keeping with the style of this lecture I want to present our experience with transition at high enthalpy in chronological order, to bring out the wild goose chase that nature has led us on, because we were slow in understanding her messages.

4.2   Slender Cone, Air and Nitrogen

One of the first experiments conducted in T5 after its completion in 1990 was an exploratory one in which we measured the heat flux distribution on a 5° half–angle cone at zero incidence in air and nitrogen flows. The heat–flux distribution enabled us to determine the transition location with good accuracy. One difficulty in comparing high–

enthalpy shock tunnel data with free–flight or cold hypersonics data is that, in order to achieve sufficiently high density for correct simulation of rate processes, the free-stream Mach number is significantly lower, and therefore the free-stream temperature is significantly higher. However, within the boundary layer the properties are the same. We therefore base our comparisons not on the free–stream Reynolds number, but on the Reynolds number Re^*, evaluated at the so–called reference temperature, representative of conditions in the laminar boundary layer.

The results of these measurements are shown in figure 16 showing a plot of the value of Re^* at transition against the specific reservoir enthalpy. The increase of Re^*_{tr} with h_0
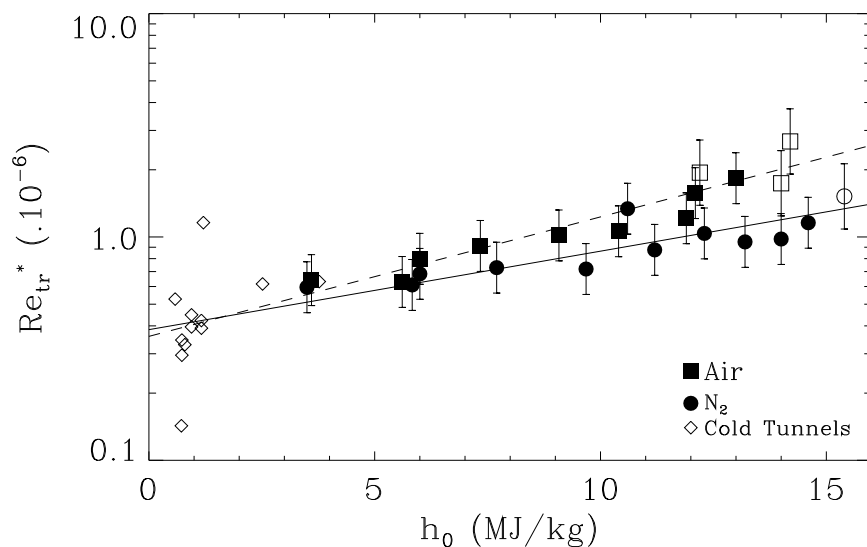

Figure 16: Transition Reynolds number Re^*_{tr} as measured in cold facilities (open diamonds), air in T5 (squares), nitrogen in T5 (circles). The open squares and circles show the value of Re^*_{tr} at the trailing edge of the cone, because in these cases no transition was observed, indicating that the transition Reynolds number is higher than the value shown. Note that the results agree reasonably well with the cold tunnel data, but that increasing h_0 increases Re^*_{tr}, slightly more so in air than in nitrogen. From Germain and Hornung (1997).

and the slight difference between air and nitrogen suggested that we were dealing with a phenomenon related to the peculiarities of these gases at high temperature.

Germain and Hornung (1997) also obtained good images of the transitional and turbulent boundary layer. From these we incorrectly speculated that the instability responsible for transition was the Tollmien–Schlichting instability.

4.3   Slender Cone, Carbon–Dioxide

The enthalpy dependence of transition observed in air and nitrogen prompted us to measure the effect in CO_2 flows for which we knew that vibration and chemistry show sig-
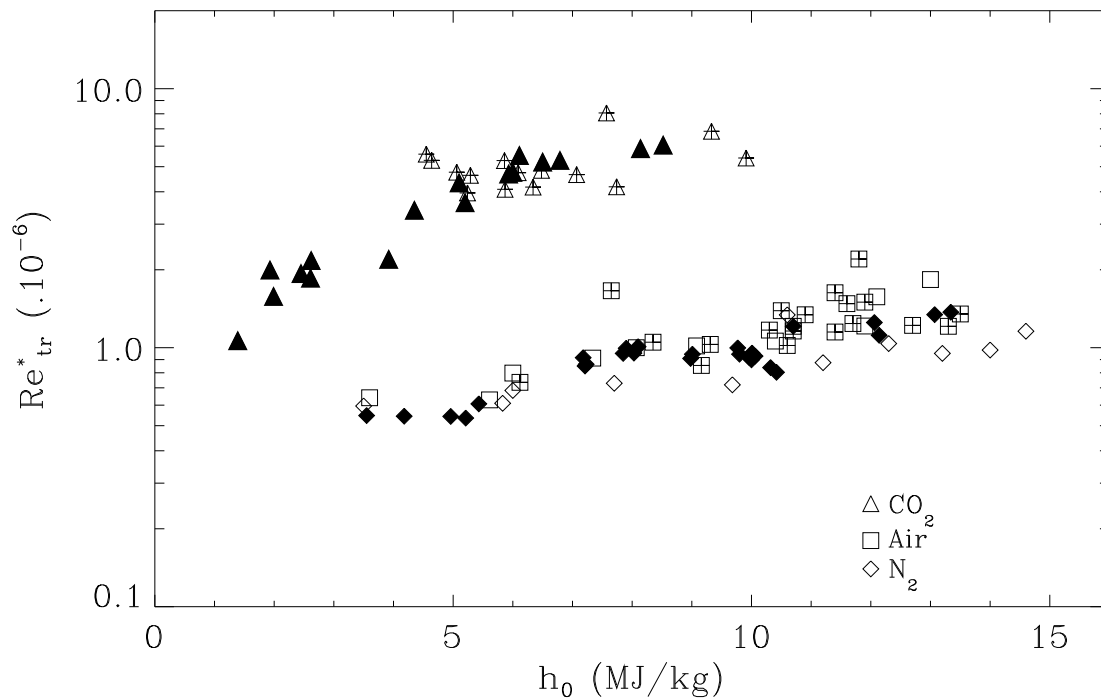
Figure 17: Plot like figure 16 including Germain and Hornung (1997)'s data as well as additional air and nitrogen data (open squares with crosses) in addition to transition data from carbon dioxide flows (triangles). The open triangles are again cases where no transition was observed on the cone. Note the large transition delay in the CO_2 flows. From Adam and Hornung (1997).

nificantly larger effects. We were not prepared, however, for the dramatic increase of the transition delay, see figure 17.

Our results prompted Johnson et al. (1998) to use their stability computations in order to check them out. An example of their results is shown in figure 18. These computations support the strong damping effect that relaxation in CO_2 flows has on the growth of disturbances and therefore on transition as observed in T5. They also showed that the acoustic mode is the mechanism by which transition is triggered at these conditions.

4.4   Mechanism

Through the work of Fujii and Hornung (2003) who studied attachment line transition in T5, we stumbled on the mechanism by which relaxation causes transition delay. It had long been known that relaxation causes damping of acoustic noise (see, *e. g.*, Clarke and McChesney (1976)). This occurs because relaxation brings about a phase lag between pressure and density fluctuations in a gas subjected to acoustic noise, with the consequence that work has to be done by the noise on the gas. The most strongly damped frequency is the inverse relaxation time, but the frequency range is quite broad. Fujii and Hornung (2003) showed that, in the case of nitrogen and air boundary layers the damping range
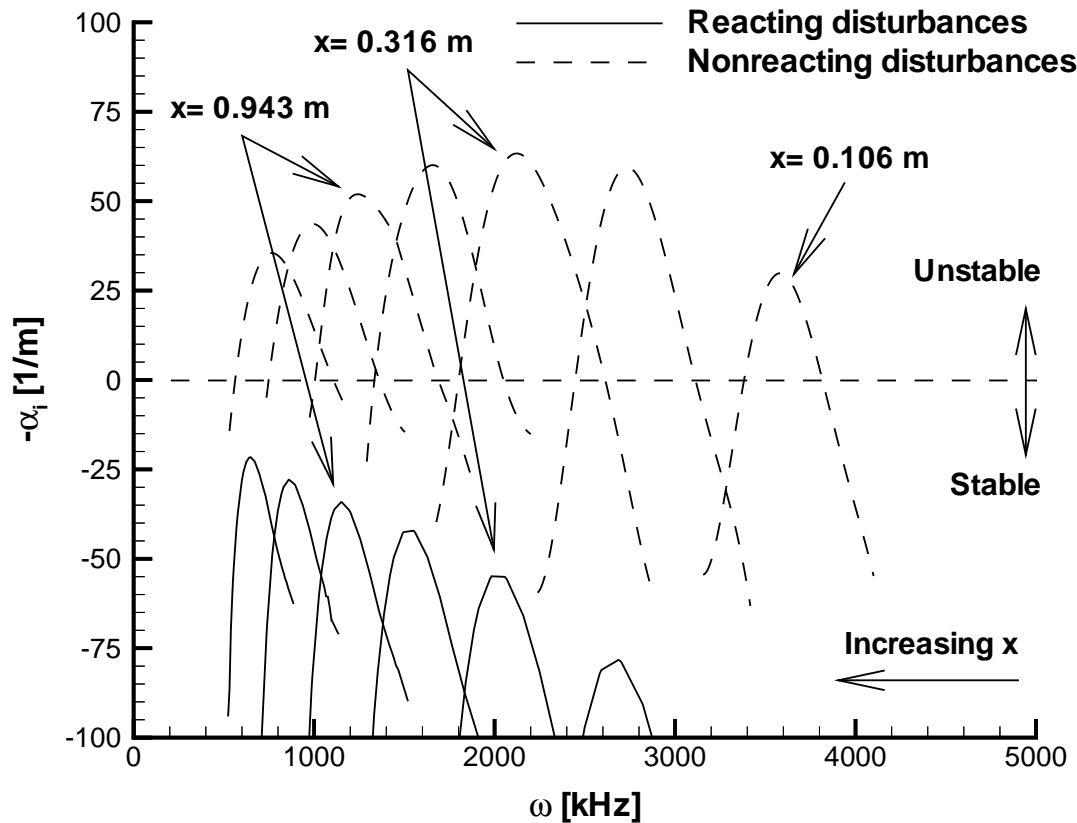
Figure 18: Plot of amplification rate ($-\alpha_i$) against disturbance frequency at different distances x from the cone tip in CO_2 flow at one of the T5 conditions. Full line: relaxation active, dashed line: relaxation switched off. The effect of relaxation is so large as to turn a boundary layer that is unstable even at the closest distance from the nose examined to one that is stable even at the largest distance from the nose examined. Note how high the most strongly amplified frequencies are. From Johnson et al. (1998).

lies quite far from the most strongly amplified frequency, while, in carbon dioxide they coincide. This explains the large difference in the relaxation effects on transition between these gases. Thus, although it was long known that hypersonic boundary layers become unstable through the acoustic Mack mode and that relaxation causes damping of acoustic noise, we did not put these two results together until nature had rubbed our noses in the evidence persistently for a large number of years.

4.5   Ongoing Work

Transition in hypersonic flow is a hot subject at present. In cold facilities, Steve Schneider and his group have compared results obtained in quiet and noisy tunnels, including measurement of Mack–mode waves. Features of such waves and their amplification have also been measured in the Technical University of Braunschweig in the Institute led by

Rolf Radespiel. At high enthalpy, efforts have been successful in the work of Hideyuki Tanno at the HIEST shock tunnel in Japan and are being started by Klaus Hannemann and his department in the HEG shock tunnel at Göttingen, Germany. A project in which carbon dioxide injection into air flows is expected to delay transition is being conducted by Ivett Leyva in T5. Graham Candler and Heath Johnson have built an impressive software system for stability computation at Minnesota, that is being used by several groups. Theoretical work by Sasha Fedorov complements these efforts. As more and more detailed investigations into the structure and growth of Mack–mode waves progress, our understanding of, and eventually our ability to predict, transition is sure to make significant strides.

4.6   Transition Control

Another phenomenon that has been known already by Kirchhoff and by Rayleigh is that acoustic noise is damped by fine blind wall porosity Sasha Fedorov and Norm Malmuth (see Fedorov et al. (2001)) had demonstrated theoretically that this principle could be applied to a hypersonic boundary layer. They initiated a project that aimed to test this idea by experiment in T5. To this end Adam Rasheed covered our slender cone with a 5 mm thick sheet of steel, which was porous on one side and non–porous on the other. The porosity consisted of holes of 50 μm diameter spaced at 100 μm, see figure 19. Rasheed et al.
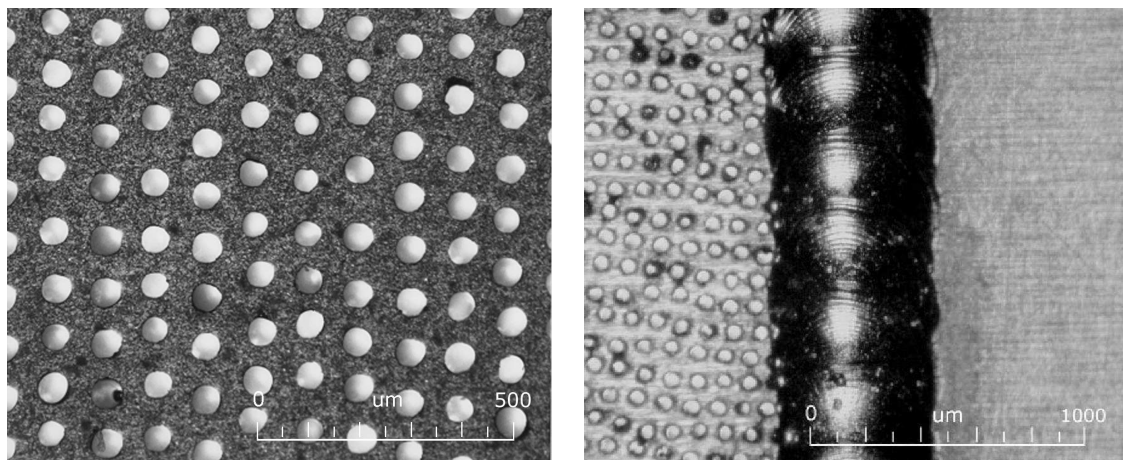

Figure 19: Left: Micrograph of the porosity of the stainless steel sheet with which the cone was covered on one side. Right: Weld of the porous to the non–porous sheet along the cone generator. From Rasheed et al. (2002).

(2002)'s measurements showed a dramatic transition delay, see figure 20 in accordance with the expectations from Fedorov et al. (2001). A very graphic demonstration is shown in the photographs of figure 21. To enable the relatively weak density gradients in a turbulent boundary layer to be brought out in a shadowgraph, a very small amount of sodium seeding is introduced in the flow, and the light source is a tunable dye laser tuned to one of the D–lines of sodium, effectively increasing the refractive index by a large factor. This method is called resonant enhancement.
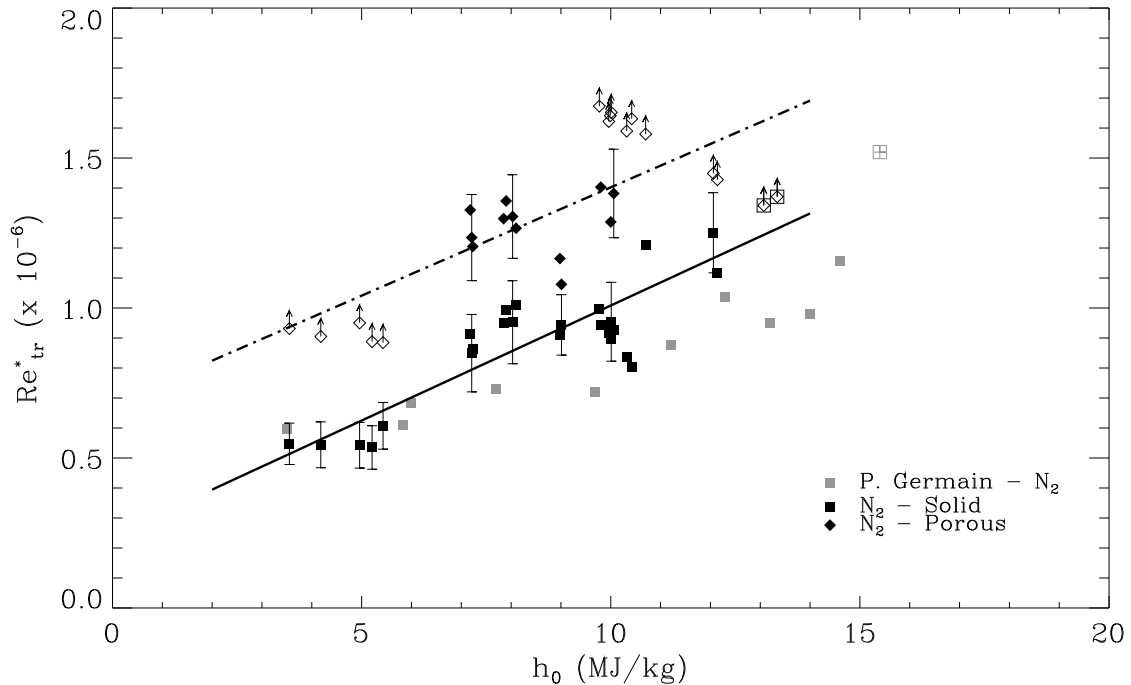
Figure 20: Transition Reynolds number on porous and solid side of the cone. The open symbols with arrows again indicate cases when no transition was observed on the cone. Note the large transition delay by porosity.
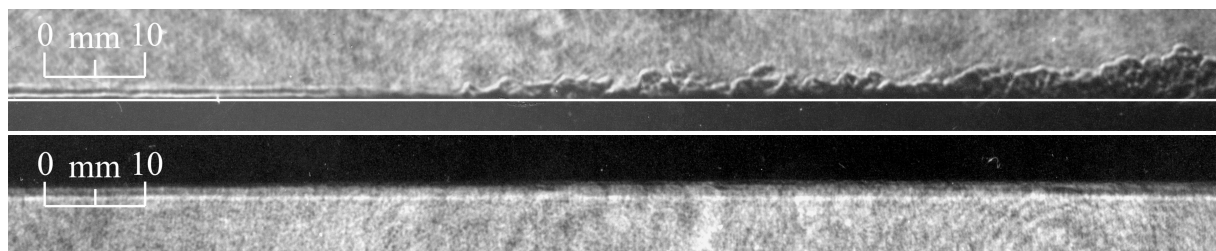

Figure 21: Top: Resonantly enhanced shadowgraph of transitional and turbulent boundary layer in a strip along the mid section of the cone on the solid side. Bottom: Strip along the porous side at the same distance from the tip of the cone. These two photos are enlargements from one run. Clearly, the boundary layer on the solid side is turbulent, while it is laminar to the end of the window on the porous side.

References

Adam, P. H. and Hornung, H. G. (1997). Enthalpy effects on hypervelocity boundary layer transition: Ground test and flight data. *J. Spacecr. Rockets*, 34:614–619.

Candler, G. V. (2010). Comparison of CFD and theoretical post–shock gradients in hypersonic flow. *Progr. Aerosp. Sc.*, 46:81–88.

Clarke, J. F. and McChesney, M. (1976). *Dynamics of Relaxing Gases.* Butterworths, London and Boston.

Fedorov, A. V., Malmuth, N. D., Rasheed, A., and Hornung, H. G. (2001). Stabilization of hypersonic boundary layers by porous coatings. *AIAA J.*, 39:605–610.

Fujii, K. and Hornung, H. G. (2003). Experimental investigation of high-enthalpy effects on attachment-line boundary-layer transition. *AIAA J.*, 41:1282–1291.

Germain, P. and Hornung, H. G. (1997). Transition on a slender cone in hypervelocity flow. *Exp. Fluids*, 22:183–190.

Hornung, H. G. (1972). Non–equilibrium dissociating flow over spheres and circular cylinders. *J. Fluid Mech.*, 53:149–176.

Hornung, H. G. (2010). Deriving features of reacting hypersonic flow from gradients at a curved shock. *AIAA Journal*, 48:287–296.

Hornung, H. G. and Houwing, A. F. P. (1980). Shock detachment from cones in a relaxing gas. *J. Fluid Mech.*, 101:307–309.

Hornung, H. G. and Lemieux, P. (2001). Shock layer instability near the Newtonian limit of hypervelocity flows. *Phys. Fluids*, 13:2394–2402.

Hornung, H. G. and Smith, G. H. (1979). Influence of relaxation on shock detachment. *J. Fluid Mech.*, 93:225–239.

Johnson, H. B., Seipp, T., and Candler, G. V. (1998). Numerical study of hypersonic reacting boundary layer transition on cones. *Phys. Fluids*, 10:2676–2685.

Leyva, I. A. (1999). *Shock detachment process on cones in hypervelocity flow*. PhD thesis, California Institute of Technology.

Mack, L. M. (1969). Boundary layer stability. Technical Report 900-277 Rev. A, Jet Propulsion Laboratory, Pasadena, California.

Malik, M. R. and Anderson, E. C. (1991). Real gas effects on hypersonic boundary-layer stability. *Phys. Fluids A*, 3:803–821.

Rasheed, A., Hornung, H. G., Fedorov, A. V., and Malmuth, N. D. (2002). Experiments on passive hypervelocity boundary-layer control using an ultrasonically absorptive surface. *AIAA J.*, 40:481–489.

Reshotko, E. (1976). Boundary–layer stability and transition. *Ann. Rev. Fluid Mech.*, 8:311–346.

Sanderson, S. R. (1995). *Shock wave interaction in hypervelocity flow*. PhD thesis, California Institute of Technology.

Sanderson, S. R., Hornung, H. G., and Sturtevant, B. (2004). The influence of non-equilibrium dissociation on the flow produced by shock impingement on a blunt body. *J. Fluid Mech.*, 516:1–37.

Stuckert, G. and Reed, H. (1994). Linear disturbances in hypersonic, chemically reacting shock layers. *AIAA J.*, 32:1384–1393.

Vincenti, W. G. and Kruger, C. H. (1965). *Physical Gas Dynamics*. John Wiley and Sons, Inc.

Wen, C.-Y. and Hornung, H. G. (1995). Non-equilibrium dissociating flow over spheres. *J. Fluid Mech.*, 299:389–405.